HHS Public Access

Author manuscript

Methods Enzymol. Author manuscript; available in PMC 2024 January 01.

Published in final edited form as:

Methods Enzymol. 2023 ; 682: 289–318. doi:10.1016/bs.mie.2022.09.007.

Chemical and structural approaches to investigate PTEN function and regulation

Thibault Viennet[a,b,†], **Santiago Rodriguez Ospina**[c,d,†], **Yunqi Lu**[c,d], **Anna Cui**[c,d], **Haribabu Arthanari**[a,b,†], **Daniel R. Dempsey**[c,d,*]

[a]Department of Cancer Biology, Dana-Farber Cancer Institute, Boston, MA, United States

[b]Department of Biological Chemistry and Molecular Pharmacology, Harvard Medical School, Boston, MA, United States

[c]Department of Dermatology, Boston University School of Medicine, Boston, MA, United States

[d]Department of Pharmacology and Experimental Therapeutics, Boston University School of Medicine, Boston, MA, United States

Abstract

Phosphatase and tensin homolog is a lipid phosphatase that serves as the major negative regulator of the PI3K/AKT pathway. It catalyzes the 3′-specific dephosphorylation of phosphatidylinositol (3,4,5)-trisphosphate (PIP_3) to generate PIP_2. PTEN's lipid phosphatase function depends on several domains, including an N-terminal segment spanning the first 24 amino acids, which results in a catalytically impaired enzyme when mutated. Furthermore, PTEN is regulated by a cluster of phosphorylation sites located on its C-terminal tail at Ser380, Thr382, Thr383, and Ser385, which drives its conformation from an open to a closed autoinhibited but stable state. Herein, we discuss the protein chemical strategies we used to reveal the structure and mechanism of how PTEN's terminal regions govern its function.

1. Introduction

Phosphatase and tensin homolog (PTEN) is one of the most mutated tumor suppressors in cancer, such as glioblastoma, breast, prostate, lung, colon, etc. (Abdulkareem & Blair, 2013; Chalhoub & Baker, 2009; Li et al., 1997). It is a lipid phosphatase that catalyzes the 3′-specific dephosphorylation of phosphatidylinositol (3,4,5)-trisphosphate (PIP_3) to generate PIP_2 (Maehama & Dixon, 1998; Worby & Dixon, 2014). By way of its enzymatic function, PTEN serves to negatively regulate the PI3K/AKT pathway by lowering the cellular pool of PIP_3, which puts a molecular brake on cell growth and proliferation (Worby & Dixon, 2014). As a result, activation of the protein kinase, AKT, is decreased, which requires PIP_3 at the plasma membrane to be activated by PDK1 and mTORC2 (Alessi, Kozlowski, Weng, Morrice, & Avruch, 1998; Chu et al., 2018; Sarbassov, Guertin, Ali, & Sabatini, 2005). Since PTEN plays such a critical role in regulating this pathway, it is also the subject of tight regulation. One major way the cell regulates PTEN's function

*Corresponding author. ddempsey@bu.edu.
†These authors contributed equally.

is by post-translational modifications, which includes acetylation, oxidation, methylation, ubiquitination, SUMOylation, and phosphorylation (Feng et al., 2019; Huang et al., 2012; Kleiger, Saha, Lewis, Kuhlman, & Deshaies, 2009; Kwon et al., 2004; Trotman et al., 2007; Vazquez, Ramaswamy, Nakamura, & Sellers, 2000; Worby & Dixon, 2014). These modifications regulate every aspect of PTEN's cellular function, yet the mechanism for their regulation is not well understood.

PTEN is 403 residues long and can be divided into three functional domains including an N-terminal catalytic domain (aa 1–186), a C2 domain (aa 187–352), and a disordered C-terminal tail (aa 353–403). A pioneering X-ray crystal structure showed that the catalytic and C2 domains are closely connected; however, the structure is missing key information about three regions critical for PTEN's function and regulation: the first 13 amino acids of the N-terminus, an internal D-loop (aa 286–309), and the full 50 amino acid C-terminal tail (Lee et al., 1999). The N-terminal domain (aa 1–24) is a polybasic region that contributes to PTEN's binding to the plasma membrane and enzymatic function, whereas the C-terminal tail is an intrinsically disordered acidic domain that is phosphorylated at multiple sites and governs its localization, activity, and stability (Bolduc et al., 2013; Chen, Dempsey, et al., 2016; Chen, Thomas, et al., 2016; Das, Dixon, & Cho, 2003; Dempsey, Jiang, Kalin, Chen, & Cole, 2018; Leslie & Downes, 2004; Nguyen et al., 2014; Rahdar et al., 2009; Vazquez et al., 2000). Within the C-terminal domain there is a cluster of phosphorylation sites at Ser380, Thr382, Thr383, and Ser385, that serve to inhibit PTEN's enzymatic function, reduce its binding to the plasma membrane, and increase its cellular stability (Bolduc et al., 2013; Chen, Dempsey, et al., 2016; Dempsey et al., 2018, 2021; Henager et al., 2016). Although phosphorylation serves a critical role in PTEN biology, the structural and mechanistic basis for its regulation was not well understood. Therefore, we used a combination of protein semi-synthesis, X-ray crystallography, biophysical methods, macromolecular NMR, molecular modeling, and enzymology to gain a more detailed understanding of how the tail of PTEN guide its cellular function and regulation (Dempsey et al., 2021). Herein, we will discuss the methods that were used to interrogate PTEN's function and regulation in greater detail and what we learned from our investigation.

2. Biochemical assays to determine the conformational state of PTEN

Phosphorylation of its C-terminal tail drives PTEN from an open to a closed conformational state, where its enzymatic activity, localization, and stability are all regulated (Bolduc et al., 2013; Chen, Dempsey, et al., 2016; Dempsey et al., 2018, 2021; Henager et al., 2016). In order to assess the structural basis for how the tail engages PTEN in the closed conformation, we used a set of biochemical assays that reliably report on the open/closed status. These included an enzymatic assay using soluble diC_6PIP_3, an assay that measures the sensitivity of the phospho-C-tail to dephosphorylation by alkaline phosphatase, and a direct trans-binding (intermolecular) assay that uses a fluorescently labeled tetraphosphorylated C-terminal tail peptide to measure the binding affinity of the tail to the core of PTEN.

Our enzymatic assay measures the rate of dephosphorylation of the 3′-phosphate of diC_6PIP_3 by PTEN using the malachite green assay (see reagents and procedure; Tables

1 and 2) (Bolduc et al., 2013; Dempsey & Cole, 2018). This assay showed that when the C-terminal tail is tetraphosphorylated, PTEN is autoinhibited with a k_{cat}/K_m decrease of >10-fold (Chen, Dempsey, et al., 2016; Chen, Thomas, et al., 2016; Henager et al., 2016), thus providing a means to assess the conformational status of the tail. Furthermore, we showed that no specific phosphorylation site dominates the commitment to the autoinhibited state; instead, each site provides a similar degree of engagement with the core of PTEN (Chen, Dempsey, et al., 2016; Dempsey et al., 2021; Henager, Henriquez, Dempsey, & Cole, 2020). This assay was also used to analyze site-directed mutants designed to open the conformation of PTEN independent of C-terminal phosphorylation and to assess how cancer mutations influence its catalytic behavior.

The alkaline phosphatase sensitivity assay (see reagents and procedure, Tables 1 and 3) measures the rate of dephosphorylation of PTEN's C-terminal tail using an antibody that is specific for the phospho-cluster (Bolduc et al., 2013; Dempsey & Cole, 2018). When the tail is in the closed conformation, the C-tail phosphates engage the core of PTEN, thus shielding them from alkaline phosphatase and its dephosphorylation; however, when PTEN is in the open state, the phosphates are more exposed, increasing their rate of hydrolysis. Using this simple assay, we were able to probe the conformational status of PTEN and mutants designed to disrupt this interaction. We also validated that the antibody specifically reports on the phosphorylation status of Ser380 for the semi-synthetic PTEN with a Y379C mutation (Chen, Dempsey, et al., 2016), but later learned that the antibody also recognizes the phosphorylation of Thr383 and Ser385 in the unscarred wild-type sequence (Henager et al., 2020).

Our direct binding assay takes advantage of a synthetic fluorescein-labeled tetraphosphorylated C-tail peptide (F-4p-18mer-tail: CpSDpTpTDpSDPENEPFDEDK$_{fluorescein}$G) generated by Fmoc solid phase peptide synthesis to measure the binding affinity of the tail to PTEN (see reagents and procedure, Tables 1 and 4) (Bolduc et al., 2013; Dempsey et al., 2021). This assay measures the change in fluorescence anisotropy of the tail peptide after a higher molecular weight complex is formed when associated with PTEN. We used this assay to measure the binding affinity of the phosphorylated tail to wild-type and mutant PTENs or VSP and to learn more about the individual phosphorylation sites' commitment to the closed-conformation. We used an anisotropy binding buffer of 50mM Tris pH8.0, 50mM NaCl and 1mM TCEP to limit the salt-dependent weakening of the tail-PTEN interaction and to mimic macromolecular NMR conditions. Binding affinities were determined by holding F-4p-18mer-tail ligand constant at 50nM and varying the concentration of protein (PTEN or VSP) and then measuring the change in fluorescence anisotropy at 23°C (EX: 495nm; EM: 520nm). Since the K_d of the proteins were saturating as compared to the concentration of the F-4p-18mer-tail peptide ligand, the data was fit to the hyperbolic plot in Eq. (1):

$$Y = B_{max}X/(K_d + X) \quad (1)$$

3. Structural basis for N-terminal function and regulation

3.1 Production of semi-synthetic PTENs for protein X-ray crystallography

We were interested in exploring the spacer region between the end of the C2 domain (Glu350) and the first phosphorylated residue (pSer380) to assess the distance required for the tail to reach its conformationally closed position (Dempsey et al., 2021). Furthermore, we wanted to use these new constructs to determine new structures of PTEN with the phosphorylated tail. Therefore, we generated a PTEN construct, which we called crPTEN, that resembles the originally crystallized version (residues 7–353 with the internal D-loop deleted from amino acids 286–309). Our construct was engineered with an artificial spacer of various lengths and a C-terminal tail of different lengths and phosphorylation status (Table 5). We generated these PTEN constructs by expressed protein ligation (EPL) to chemically ligate the synthetic peptide tails (see reagents and procedure, Tables 6 and 7) (Bolduc et al., 2013; Dempsey & Cole, 2018; Dempsey et al., 2021; Muir, Sondhi, & Cole, 1998). EPL is a protein semi-synthetic method that chemically connects two protein components by native chemical ligation (Dawson, Muir, Clark-Lewis, & Kent, 1994; Muir et al., 1998). This method can be used to install additional chemical functionality onto proteins, such as PTMs. For C-terminal ligations (Fig. 1A and B), we expressed crPTEN with an GyrA intein fused to the C-terminal end which catalyzes the formation of a reversible thioester between the C-terminus of the protein and the N-terminus of the intein. We then cleave the intein from PTEN by incubating it with 2-mercaptoethane sulfonate (MESNa) through a transthioesterification reaction to generate a PTEN-MESNa thioester. Then an N-terminal Cys-containing synthetic peptide is ligated to the newly formed PTEN-MESNa thioester by a second transthioesterification reaction, followed by an intramolecular rearrangement to form a peptide bond between PTEN and the synthetic C-tail peptide. Moreover, the artificial spacer was designed to be flexible so that the tail can reach its closed position and reduce heterogeneity of other PTMs naturally found in this region that may hinder crystal growth (Bolduc et al., 2013; Miller, Lou, Seldin, Lane, & Neel, 2002). We define the spacer group as any amino acid after Glu353 until the first phosphorylated residue, Ser380 (Dempsey et al., 2021). We measured the degree of autoinhibition of all these crPTENs using our diC_6PIP_3 enzymatic assay to determine special distance constraints imposed by the linker for the tail to reach its conformationally closed site. We determined that the minimal distance required for the tail to reach its autoinhibitory conformation is 65Å, which is fully consistent with previous biochemical and structural data (Bolduc et al., 2013; Chen, Dempsey, et al., 2016; Dempsey et al., 2018, 2021; Henager et al., 2016; Masson, Perisic, Burke, & Williams, 2016). We were also able to crystalize four of these constructs (Table 5), which resolved new structural details of the N-terminal region (aa 7–14) that are critical for catalysis and plasma membrane binding (Campbell, Liu, & Ross, 2003; Dempsey et al., 2021; Iijima, Huang, Luo, Vazquez, & Devreotes, 2004; Walker, Leslie, Perera, Batty, & Downes, 2004). Prior to crystallization, these proteins were purified over a size exclusion chromatography column using a final buffer of 50mM Tris pH8.0, 200mM NaCl, 10mM DTT and concentrated to 14–20mg/mL (see procedure, Table 7). Hanging drop crystal trays were set for crPTEN and tetraphosphorylated crPTENs with a spacer of 13 residues by adding equal volume of 14mg/mL crPTEN to 100mM Bis-Tris propane pH7.0, 1.2M DL-Malic acid, and incubated at 20 °C for a week. Crystals for

tetraphosphorylated crPTEN with spacers of 20 and 22 residues were generated by the same method but by using 300mM sodium citrate tribasic and 20% (*v*/v) PEG 3350.

3.2 X-ray crystal structure of PTEN revealing N-terminal segment of PTEN

We determined the structure of four crPTEN constructs (Table 5), which were composed of several spacers and C-tails (Dempsey et al., 2021). The structure of 4p-crPTEN-13sp-T2 (PDB: 7JUK) was the first to be determined, where we unexpectedly observed a N-terminal α-helix (residues 7–14). Our enzymatic assay showed that 4p-crPTEN-13sp-T2 was fully active and the N-terminal helix was also present in the unphosphorylated crPTEN structure (n-crPTEN-13sp-T1; PDB: 7JUL) (Fig. 2A); therefore, we surmised that the N-terminal helix did not form due to PTEN being in an autoinhibited state. Furthermore, the structures of the constructs that were autoinhibited by the ligated phosphorylated tail (4p-crPTEN-20sp-T3; PDB: 7JVX and 4p-crPTEN-22sp-T3; PDB: 7JTX) showed a greater loss of density for the N-terminal region as we increased the spacer length. This indicated that the phosphorylated tail might be influencing the conformation of the N-terminal region by driving it to a more disordered state.

Our new structure shows that the N-terminal helix is next to the active site and makes direct contacts with the P-loop that contains PTEN's catalytic cysteine (Cys124) (Dempsey et al., 2021). The helix is stabilized by an extensive network of hydrogen bonds (Fig. 2B), where several of the key residues are also mutated in cancer, suggesting that the position of the helix is critical for PTEN's tumor-suppressing function. We tested the importance of this helix for the catalytic function of PTEN and cancer by generating point mutations (S10R, R15I, and D24V) that would disrupt key interactions that stabilize its position. We also evaluated a helix-breaking proline mutation (S10P). Our new structure showed that Arg15 bridges Asp22 to Ser10 and Asp24 create a salt bridge with Lys13 and Arg159 (Fig. 2B). Using our enzymatic di$C_6$$PIP_3$ assay, we determined that all these mutations made PTEN catalytically impaired, with S10R, S10P, and R15I all having an elevated K_m, and D24V being completely devoid of catalytic activity under our standard assay conditions. These data demonstrate the critical nature of the N-terminal α-helix in PTEN's enzymatic activity, where mutations that disrupt its key interactions can lead to a decrease in PTEN's lipid phosphatase and tumor-suppressing function.

3.3 Production of semi-synthetic N-terminally labeled PTEN for macromolecular NMR

The N-terminal 16 amino acids serve an important role in PTEN's enzymatic activity and plasma membrane binding, where mutation of key residues that stabilize the positioning of the helix leads to a more catalytically deficient enzyme (Dempsey et al., 2021). Furthermore, the N-terminal segment abuts the active site, where our structural and biochemical data has also positioned the phosphorylated tail (Chen, Dempsey, et al., 2016; Dempsey et al., 2018, 2021); therefore, we sought to determine how the phosphorylated tail may influence this segment (Dempsey et al., 2021). We used macromolecular NMR to gain insight into the N-terminal segment (amino acids 1–16), since we were unable to determine an X-ray crystal structure that shows the positioning of the tail. In order to install the isotopes necessary to visualize this segment by NMR, we expressed PTEN in two parts and then chemically ligated them using expressed protein ligation (Fig. 1C). The first 16 amino acids were made

in *E. coli*, whereas the remaining part of PTEN (amino acids 17–378) was generated in High Five insect cells (see reagents and procedure, Tables 8 and 9). The first 16 amino acids of PTEN were fused with an N-terminal 8×-His-SUMO tag and a C-terminal GyrA intein and chitin-binding domain (8× His_{tag}-SUMO-$PTEN_{1–16}$-GryA intein-CBD) for purification and eventual generation of a C-terminal thioester for ligations to the remaining part of PTEN. We expressed this segment using *BL21(DE3) Rosetta pLysS E. coli cells* in minimal media supplemented with 1g/L [^{15}N] ammonium chloride to make the first 16 amino acids of PTEN labeled with ^{15}N for NMR.

The other segment of PTEN (PTEN-NΔ16$_{Q17C,\ Y379C}$) was expressed in High Five insect cells fused with an N-terminal 8×-His-$SUMO_{star}$ tag and a C-terminal GyrA intein and chitin-binding domain (CBD) for purification. $SUMO_{star}$ was used instead of SUMO to protect the tag from being removed by endogenous deSUMOylases in insect cells (Dempsey et al., 2021). After the initial purification of both pieces (see reagents and procedure, Tables 8 and 9), the two components were ligated together using expressed protein ligation to generate ^{15}N-aa1–16-ss$PTEN_{Q17C}$. We demonstrated that the Q17C has no impact on the binding of the phosphorylated tail to PTEN. With the segmentally labeled PTEN in hand, we assigned the ^{15}N-^{1}H HMQC resonances of amino acids Ile4-Ser10 and Lys13. We then monitored how the NMR resonances were affected by adding the phosphorylated tail peptide. We observed global chemical shift perturbations when the phosphorylated tail was present, indicating that the phosphorylated tail has a significant influence on the conformation of the N-terminus. We then compared these ^{15}N-^{1}H HMQC NMR spectra with the free N-terminal peptide, which showed the peaks in the phospho-tail ^{15}N-^{1}H HMQC NMR spectrum shifting in the same direction and manner as the free N-terminal peptide, meaning that when PTEN's C-tail is phosphorylated, the N-terminus adopts a similar disordered conformation as the free peptide. Therefore, phosphorylation of PTEN's C-terminal tail causes the N-terminal helix to melt and adopt a more disordered state. This shift to a more disordered state likely disrupts some of the key contacts of the N-terminus, perhaps contributing to its autoinhibited state, as observed with our mutagenesis experiments.

4. Structural basis for regulation of PTEN by C-terminal phosphorylation

4.1 Production of VSP for macromolecular NMR experiments

4.1.1 Isotopically labeling VSP for NMR assignments—The *Ciona intestinalis* voltage-sensing phosphatase (VSP) construct of the catalytic and C2 domains (aa 241–576) was cloned into a pET28b(+) vector with an N-terminal 8×-His-SUMO tag that can be efficiently cleaved off with ULP1 protease. VSP was expressed in BL21(DE3) Rosetta pLysS *E. coli* cells grown in deuterated M9 minimal medium (see Table 10). VSP was purified as described in Dempsey et al. (2021). The final yield of ^{2}H-^{13}C-^{15}N-VSP was about 2mg/L culture which translated into samples of approximately 180 μM packed into 5mm Shigemi tubes (280μL).

Initially, the buffer conditions were screened using Differential Scanning Fluorescence (DSF) and NMR was performed to narrowed down the experimental conditions to 50mM Tris pH7.5, 50mM NaCl, 1mM TCEP and 5% *v*/v $^{2}H_2O$ at a measuring temperature of

20°C. Under these conditions the samples were stable for ca. 2days. Notably, the samples were much more stable in the presence of excess of tetra-phosphorylated C-tail.

A sample of ^{2}H-^{13}C-^{15}N VSP was used to acquire a first set of triple resonance NMR experiment for backbone assignments. Transverse relaxation optimized (TROSY) (Salzmann, Pervushin, Wider, Senn, & Wüthrich, 1998) versions of HSQC, HNCA, HN(CO)CA, HNCO and HN(CA) CB experiments were recorded. However, the number of peaks present in spectra dramatically reduced from HSQC (262 peaks of the expected 324 visible residues) to HNCA (172 peaks) and HN(CA)CB (18 peaks). One reason for the reduced number of peaks can be incomplete back-exchange of amide ^{2}H for ^{1}H in parts of VSP that are not solvent-exposed. This is usually mitigated by using high pH and temperature, which is not possible due to the low stability of VSP in these conditions. The other reason is the rather high molecular weight of VSP (38kDa, which corresponds to 43kDa at 20°C), leading to slow tumbling time and fast relaxation rates, and potential additional contributions to relaxation due to conformational exchange. The HN(CA)CB particularly suffers from this due to the long (14.4ms) magnetization transfer step from $^{13}C\alpha$ to $^{13}C\beta$ (Fig. 3).

To mitigate the relaxation problem, the more sensitive HNCA experiment was used with beta/alpha decoupling pulse approach (BADCOP) (Coote et al., 2018) was used. This method makes use of band-selective $^{13}C\beta$ decoupling pulses to encode information on $^{13}C\beta$ chemical shift in $^{13}C\alpha$ line shapes. As a result, the $^{13}C\alpha$ peak shapes in an HNCA spectrum appears either as a singlet or as a doublet, depending on the $^{13}C\beta$ chemical shift and the decoupling pulse used. This method circumvents the needs to measure insensitive HN(CA)CB experiments to gain information about amino acid types corresponding to a specific NMR spin system. The experiments use a single optimal control-derived homonuclear decoupling pulse in the middle of the $^{13}C\alpha$ evolution, thus they are as sensitive as HNCA experiments. The degeneracy between $^{13}C\alpha$ resonances, which is the major limitation in HNCA-based assignment, is circumvented by the 13Cβ-dependent peak shape modulation. The available pulses BADCOP1–3 allow clustering of peaks in 4 groups corresponding to their amino acid types: (i) Ser and Thr; (ii) LDFYNI; (iii) CMKVPRHEWQ and (iv) Ala. Gly are readily recognized due to the lack of Cβ. However, high resolution is required in the $^{13}C\alpha$ dimension of HNCA spectra, so that the 33–42Hz $^{1}J_{C\alpha\text{-}C\beta}$ splitting are observed. This translates into an evolution time of ~50ms (256 complex points), which in the case of VSP corresponds to an experimental times in the order of 40days. Such experiments are impractical without use of non-uniform sampling (NUS) techniques. Using NUS we sampled 10% of the Nyquist grid in the two indirect dimensions. The sample points were chosen using Poisson-Gap sampling (Hyberts, Milbradt, Wagner, Arthanari, & Wagner, 2012) and the spectra were subsequently reconstructed using the hmsIST (Hyberts, Robson, & Wagner, 2017) algorithm. The final measurement time was 4 days and 2h, however, while processing the data it was observed that no signal was present in the second half of the experiment due to the poor sample stability. To optimize signal-to-noise ratio, these data points were discarded, creating a 5% non-uniformly sampled experiment. This was possible because the increments were acquired in a random fashion rather than in the order of the schedule (scrambled schedule). The quality of reconstruction was acceptable, with minor reconstruction artifacts detected in the final spectra.

Following this procedure, 73 peaks (22% of VSP, 42% of the HNCA resonances) could be assigned to their corresponding residue. Due to the limited sensitivity and stability of samples, the other peaks could not be assigned. Moreover, some peaks were not assigned with high confidence due to $^{13}C\alpha$ chemical shift discrepancies that could not be resolved by comparing the different line shapes produced by the different BADCOP decoupling pulses.

To extend assignments and increase their confidence level, selective amino acid unlabeling was used. Arg and Lys (Fig. 4), Asn, His and Gln can be selectively unlabeled in *E. coli* by simple addition of non-isotope labeled amino acids in the growth medium without interference from amino acid scrambling (Dubey, Kadumuri, Jaipuria, Vadrevu, & Atreya, 2016). This made it possible to unambiguously assign amino acid types to 17 peaks, which greatly increased the confidence level of resonance assignments. Moreover, ^{15}N-VSP samples containing seven different point mutations were produced (R13G, R46G, H122G, R158A, K276G, R280G and K314A). Point mutations were chosen in segments corresponding to biologically relevant elements of PTEN (e.g., the active site, the CBR III and Cα2 segments previously suggested to interact with the tetra-phosphorylated C-tail). However, only H122 and R280 could be assigned since the other peaks were not visible on our ^{15}N-^{1}H TROSY-HSQC spectra. Ultimately, 98 resonances (30% of VSP, 57% of the HNCA resonances) could be assigned to their corresponding residue. Interestingly, only 30 resonance of the catalytic phosphatase domain were assigned, while 68 resonances were assigned in the C2 domain. This discrepancy can be explained by a more dynamic behavior of the phosphatase domain (leading to peak broadening due to conformational exchange) compared to a more rigid C2 domain.

4.1.2 Protein semi-synthesis to generate segmentally labeled phosphorylated VSP for macromolecular NMR—

We generated semi-synthetic chimeric VSPs for biochemical and NMR analysis by expressing the C-terminal PTEN homology domain of *Ciona intestinalis* VSP (amino acids 240–576) fused to a GyrA intein, a chitin-binding domain, and carrying an N-terminal 8×-His-SUMO tag in *BL21(DE3) Rosetta pLysS E. coli* cells. At first, we ligated the full-length PTEN C-terminal tetraphosphorylated tail and purified 4p-VSP with the same exact methods used to generate 4p-PTEN (see Section 3.1). Later, we found that the yield was significantly improved by: (i) codon optimization of the gene, (ii) use of an 8×-His-SUMO tag, and (iii) purification of VSP using nickel affinity chromatography prior to ligating the tail in solution (instead of ligating after immobilization to the chitin resin) (Dempsey et al., 2021). For NMR analysis of the phosphorylated tail, we expressed 8×-His-SUMO-VSP$_{C363S}$-GyrA intein-CBD in M9 minimal medium (see Table 10). We then purified the protein using nickel affinity chromatography, followed by ligation of the synthetic 18-mer tetraphosphorylated PTEN C-tail peptide by EPL and cleave of the 8×-His-SUMO with ULP1 at the same time. The newly formed 4p-VSP$_{C363S}$ was further purified by anion-exchange chromatography (MonoQ), size exclusion chromatography (Superdex200), and then dialyzed into 50mM Tris pH7.5, 50mM NaCl, 1mM TCEP (see procedure, Table 10).

4.2 Structural model for how the C-terminal tail engages VSP

At this stage of the project, we established that VSP acts as a faithful surrogate for PTEN to study the structure and mechanism of phospho-C-tail binding, as exhibited by our direct binding and alkaline phosphatase sensitivity assays (Dempsey et al., 2021). Thus, we sought to map out the interaction interface using NMR. CSPs and differences in peak intensities report on which residues are affected by interaction with the 4p-C-tail. Plotting CSPs on the primary sequence of VSP and on the crystal structure helps visualize areas of interaction. Most CSPs clustered around residues 210–220, 265–275, and 305–315 in the CBRIII and Cα2 segments, as well as some parts of the catalytic domain (e.g., 28–32 and 120–123).

CSPs are the result of a change in electronic environment of the observed nuclei in response to the addition of a potential interaction partner. However, CSPs can result from a direct interaction or from indirect effects such as allostery (Williamson, 2018). Several NMR experiments such as nuclear Overhauser effect (NOE), cross-saturation transfer (CST) (Shimada, 2005) and paramagnetic resonance enhancements (PRE) (Clore & Iwahara, 2009) provide evidence of direct interaction. No NOEs were observed between VSP and the C-tail, probably due to the inherent flexibility of the C-tail even when bound to VSP in its tetra-phosphorylated state. PRE are extremely sensitive experiments, even in cases where a small fraction of the paramagnetically-labeled protein is bound in the NMR timescale. Indeed, PREs could be observed for residues in the C2 domain of VSP. Since the paramagnetic tag was introduced right before the phosphorylation sites, it can be concluded that the phosphates anchor the C-tail on the C2 domain, while the later residues of the C-tail would contact the catalytic domain. We also leveraged tri-phosphorylated peptides with the thought that deleting a phosphate at each individual site should result in unique chemical shift perturbations that pinpoint the position of that phosphate. This is indeed what we observed, where unique CSPs for pSer380 and pThr382 occurred in the CBRIII loop and pThr383 and pSer385 in the Cα2 segment.

We were interested in generating an ensemble of models that paints a portrait of how the phosphorylated tail engages with VSP/PTEN that is consistent with our biochemical and structural data. Therefore, we started with building models using the FloppyTail tool in Rosetta (Fig. 5) (Kleiger et al., 2009; Santiago-Frangos, Jeliazkov, Gray, & Woodson, 2017). First, a random ensemble of 10,000 conformations of the C-tail was generated from a tail built-in extended conformation followed by short, simulated annealing steps, to optimize sampling of dihedral angles (low resolution stage). Then, all side chain atoms were introduced using PyRosetta, including the four phosphorylated side chains, and the resulting 10,000 conformers were used as seeds for a high-resolution simulated annealing stage that allows conformers to sample the potential interaction interface on VSP. At this stage, the atomic contacts that were enriched in the top 100 structures compared to the rest of the 10,000 conformers were analyzed. Notably, the CBRIII and Cα2 segments were found as the main interaction sites, in line with our experimental data.

Lastly, to produce a model that best recapitulates the interaction and can act as a model to help rationalize biological findings, further experiments and future drug design efforts, data-driven molecular docking was used. Chemical shift perturbations were filtered out if the corresponding C2 domain residue did not exhibit paramagnetic relaxation enhancement

(they can likely be attributed to allosteric effects) and used as a network of ambiguous restraints. Additionally, a set of restraints corresponding to the experimental cross-links was added (Chen, Dempsey, et al., 2016), and the backbone and side chain conformations of the 4p-C-tail and interaction interface on VSP were allowed flexibility. Molecular docking using Haddock (van Zundert et al., 2016) was performed using solvated docking, flexible refinement, and short molecular dynamic simulations in explicit solvation shells for the top 10 lowest energy conformers derived from FloppyTail. The model with the lowest Haddock score was considered the final, most representative conformation of a narrow ensemble of low-energy states adopted by the 4p-C-tail bound to VSP. As expected, the four phosphorylation sites anchor the C-tail on the C2 domain by a network of electrostatic interactions with Arg and Lys residues in the CBRIII and Cα2 segments. Interestingly, it was also observed that the later acidic parts of the C-tail contact the catalytic domain, including Glu390 interacting with two Lys residues in the active site. When testing Asp mutants of the VSP active site Lys residues (Lys364 and Lys 367), we observed a significant weakening of the phospho-tail interaction (3.4-fold), thus validating their importance to the assembly of the closed conformation. Furthermore, mutations of basic residues in the CBRIII and Cα2 segments resulted in a more dramatic weakening of phospho-tail binding to PTEN, as predicted by our model.

5. Summary and future directions

Protein semi-synthesis methods to generate several different versions of phosphorylated PTEN and VSP were vital in unraveling the mechanistic and structural basis for how phosphorylation regulates PTEN's function. We used a combination of protein semi-synthesis, protein crystallography, macromolecular NMR, computational modeling, site-directed mutagenesis, and photo-crosslinking mass spectrometry to determine that the phosphorylated tail acts as a belt that wraps around the C2 domain with the phosphates engaging with the CBRIII loop and Cα2 segment, while the later acidic segments of the tail extend into the phosphatase domain making contacts with and around the active site (Dempsey et al., 2021). Previous mutagenesis experiments highlight the importance of these regions to phospho-tail binding, but their direct roles remained inconclusive (Mingo et al., 2019). The structural portrait generated by our investigation provides a more detailed mechanism for how the phosphorylated tail associates with PTEN to autoinhibit its enzymatic function and weaken its binding to the plasma membrane. It does this by masking the surfaces critical to these functions, essentially behaving as a molecular mimic of the negatively charged plasma membrane itself.

We also determined a new structure of PTEN, where its N-terminal region adopts an α-helix, which is critical for PTEN's enzymatic function. This is a dynamic region that transitions to a more disordered state in the presence of the phosphorylated tail, as shown in our NMR data (Dempsey, 2021). Disrupting key contacts of this helix by cancer mutations or the phosphorylated tail results in PTEN being more catalytically impaired.

Future work to understand the regulatory mechanisms of other PTMs in the C-terminal tail or in the N-terminal segment of PTEN, such as ubiquitination of Lys13 will lead to a more comprehensive understanding of how the cell governs PTEN's biological function and

how diseases such as cancer exploit these mechanisms for its benefit (Fusco et al., 2020). Furthermore, our new structural portrait may shed some light on how phosphorylation of PTEN enhances its stability in the cell by evading ubiquitination by the E3 ligase, WWP2 (Chen et al., 2017; Dempsey et al., 2018; Li et al., 2018; Maddika et al., 2011).

Finally, our work emphasizes the power of expressed protein ligation with understanding the regulatory mechanisms of PTMs. We hope this manuscript provides a blueprint for other investigators to address these important questions.

Acknowledgments

We thank NIH R00GM130961 (D.R.D.) for financial support.

Abbreviations

CBD	chitin-binding domain
CSPs	chemical shift perturbations
CST	cross-saturation transfer
NMR	nuclear magnetic resonance
NOE	nuclear overhauser effect
PIP2	phosphatidylinositol 4,5-bisphosphate
PIP3	phosphatidylinositol (3,4,5)-trisphosphate
PTEN	phosphatase and tensin homolog
PTMs	post-translational modifications
VSP	voltage-sensing phosphatase

References

Abdulkareem IH, & Blair M (2013). Phosphatase and tensin homologue deleted on chromosome 10. Nigerian Medical Journal: Journal of the Nigeria Medical Association, 54(2), 79–86. 10.4103/0300-1652.110033. [PubMed: 23798791]

Alessi DR, Kozlowski MT, Weng QP, Morrice N, & Avruch J (1998). 3-Phosphoinositide-dependent protein kinase 1 (PDK1) phosphorylates and activates the p70 S6 kinase in vivo and in vitro. Current Biology: CB, 8(2), 69–81. 10.1016/s0960-9822(98)70037-5. [PubMed: 9427642]

Bolduc D, Rahdar M, Tu-Sekine B, Sivakumaren SC, Raben D, Amzel LM, Devreotes P, Gabelli SB, & Cole P (2013). Phosphorylation-mediated PTEN conformational closure and deactivation revealed with protein semisynthesis. eLife, j2, e00691. doi:10.7554/eLife.00691.

Campbell RB, Liu F, & Ross AH (2003). Allosteric activation of PTEN phosphatase by phosphatidylinositol 4,5-bisphosphate. The Journal of Biological Chemistry, 278, 33617–33620. [PubMed: 12857747]

Chalhoub N, & Baker SJ (2009). PTEN and the PI3-kinase pathway in cancer. Annual Review of Pathology, 4, 127–150.

Chen Z, Dempsey DR, Thomas SN, Hayward D, Bolduc DM, & Cole PA (2016). Molecular features of phosphatase and tensin homolog (PTEN) regulation by C-terminal phosphorylation. The Journal of Biological Chemistry, 291(27), 14160–14169. 10.1074/jbc.M116.728980. [PubMed: 27226612]

Chen Z, Jiang H, Xu W, Li X, Dempsey DR, Zhang X, et al. (2017). A tunable brake for HECT ubiquitin ligases. Molecular Cell, 66(3), 345–357.e6. 10.1016/j.molcel.2017.03.020. [PubMed: 28475870]

Chen Z, Thomas SN, Bolduc DM, Jiang X, Zhang X, Wolberger C, et al. (2016). Enzymatic analysis of PTEN ubiquitylation by WWP2 and NEDD4–1 E3 ligases. Biochemistry, 55(26), 3658–3666. 10.1021/acs.biochem.6b00448. [PubMed: 27295432]

Chu N, Salguero AL, Liu AZ, Chen Z, Dempsey DR, Ficarro SB, et al. (2018). Akt kinase activation mechanisms revealed using protein semisynthesis. Cell, 174(4), 897–907.e14. 10.1016/j.cell.2018.07.003. [PubMed: 30078705]

Clore GM, & Iwahara J (2009). Theory, practice, and applications of paramagnetic relaxation enhancement for the characterization of transient low-population states of biological macromolecules and their complexes. Chemical Reviews, 109(9), 4108–4139. 10.1021/cr900033p. [PubMed: 19522502]

Coote PW, Robson SA, Dubey A, Boeszoermenyi A, Zhao M, Wagner G, et al. (2018). Optimal control theory enables homonuclear decoupling without Bloch-Siegert shifts in NMR spectroscopy. Nature Communications, 9(1), 3014. 10.1038/s41467-018-05400-4.

Das S, Dixon JE, & Cho W (2003). Membrane-binding and activation mechanism of PTEN. Proceedings of the National Academy of Sciences of the United States of America, 100, 7491–7496. [PubMed: 12808147]

Dawson PE, Muir TW, Clark-Lewis I, & Kent SB (1994). Synthesis of proteins by native chemical ligation. Science (New York, N.Y.), 266(5186), 776–779. 10.1126/science.7973629. [PubMed: 7973629]

Dempsey DR, & Cole PA (2018). Protein chemical approaches to understanding PTEN lipid phosphatase regulation. Methods in Enzymology, 607, 405–422. 10.1016/bs.mie.2018.05.007. [PubMed: 30149868]

Dempsey DR, Jiang H, Kalin JH, Chen Z, & Cole PA (2018). Site-specific protein labeling with N-hydroxysuccinimide-esters and the analysis of ubiquitin ligase mechanisms. Journal of the American Chemical Society, 140(30), 9374–9378. 10.1021/jacs.8b05098. [PubMed: 30016585]

Dempsey DR, Viennet T, Iwase R, Park E, Henriquez S, Chen Z, et al. (2021). The structural basis of PTEN regulation by multi-site phosphorylation. Nature Structural & Molecular Biology, 28(10), 858–868. 10.1038/s41594-021-00668-5.

Dubey A, Kadumuri RV, Jaipuria G, Vadrevu R, & Atreya HS (2016). Rapid NMR assignments of proteins by using optimized combinatorial selective unlabeling. Chembiochem: a European journal of chemical biology, 17(4), 334–340. 10.1002/cbic.201500513. [PubMed: 26662553]

Feng J, et al. (2019). PTEN arginine methylation by PRMT6 suppresses PI3K-AKT signaling and modulates pre-mRNA splicing. Proc. Natl. Acad. Sci. USA, 116, 6868–6877. [PubMed: 30886105]

Fusco N, Sajjadi E, Venetis K, Gaudioso G, Lopez G, Corti C, et al. (2020). *PTEN* alterations and their role in cancer management: Are we making headway on precision medicine? Genes, 11(7), 719. 10.3390/genes11070719. [PubMed: 32605290]

Henager SH, Chu N, Chen Z, Bolduc D, Dempsey DR, Hwang Y, et al. (2016). Enzyme-catalyzed expressed protein ligation. Nature Methods, 13(11), 925–927. 10.1038/nmeth.4004. [PubMed: 27669326]

Henager SH, Henriquez S, Dempsey DR, & Cole PA (2020). Analysis of site-specific phosphorylation of PTEN by using enzyme-catalyzed expressed protein ligation. Chembiochem, 21, 64–68. [PubMed: 31206229]

Huang J, et al. (2012). SUMO1 modification of PTEN regulates tumori-genesis by controlling its association with the plasma membrane. Nature Communications, 3, 911.

Hyberts SG, Milbradt AG, Wagner AB, Arthanari H, & Wagner G (2012). Application of iterative soft thresholding for fast reconstruction of NMR data non-uniformly sampled with

multidimensional Poisson Gap scheduling. Journal of Biomolecular NMR, 52(4), 315–327. 10.1007/s10858-012-9611-z. [PubMed: 22331404]

Hyberts SG, Robson SA, & Wagner G (2017). Interpolating and extrapolating with hmsIST: Seeking a t_{max} for optimal sensitivity, resolution and frequency accuracy. Journal of Biomolecular NMR, 68(2), 139–154. 10.1007/s10858-017-0103-z. [PubMed: 28332026]

Iijima M, Huang YE, Luo HR, Vazquez F, & Devreotes PN (2004). Novel mechanism of PTEN regulation by its phosphatidylinositol 4,5-bisphosphate binding motif is critical for chemotaxis. The Journal of Biological Chemistry, 279, 16606–16613. [PubMed: 14764604]

Kleiger G, Saha A, Lewis S, Kuhlman B, & Deshaies RJ (2009). Rapid E2–E3 assembly and disassembly enable processive ubiquitylation of cullin-RING ubiquitin ligase substrates. Cell, 139(5), 957–968. 10.1016/j.cell.2009.10.030. [PubMed: 19945379]

Kwon J, et al. (2004). Reversible oxidation and inactivation of the tumor suppressor PTEN in cells stimulated with peptide growth factors. Proceedings of the National Academy of Sciences of the United States of America, 101, 16419–16424. [PubMed: 15534200]

Lee JO, Yang H, Georgescu MM, Di Cristofano A, Maehama T, Shi Y, et al. (1999). Crystal structure of the PTEN tumor suppressor: Implications for its phosphoinositide phosphatase activity and membrane association. Cell, 99(3), 323–334. 10.1016/s0092-8674(00)81663-3. [PubMed: 10555148]

Leslie NR, & Downes CP (2004). PTEN function: How normal cells control it and tumour cells lose it. The Biochemical Journal, 382(Pt 1), 1–11. 10.1042/BJ20040825. [PubMed: 15193142]

Li H, Zhang P, Zhang Q, Li C, Zou W, Chang Z, et al. (2018). WWP2 is a physiological ubiquitin ligase for phosphatase and tensin homolog (PTEN) in mice. The Journal of Biological Chemistry, 293(23), 8886–8899. 10.1074/jbc.RA117.001060. [PubMed: 29685889]

Li J, et al. (1997). PTEN, a putative protein tyrosine phosphatase gene mutated in human brain, breast, and prostate cancer. Science, 275, 1943–1947. [PubMed: 9072974]

Maddika S, Kavela S, Rani N, Palicharla VR, Pokorny JL, Sarkaria JN, et al. (2011). WWP2 is an E3 ubiquitin ligase for PTEN. Nature Cell Biology, 13(6), 728–733. 10.1038/ncb2240. [PubMed: 21532586]

Maehama T, & Dixon JE (1998). The tumor suppressor, PTEN/MMAC1, dephosphorylates the lipid second messenger, phosphatidylinositol 3,4,5-trisphosphate. The Journal of Biological Chemistry, 273(22), 13375–13378. 10.1074/jbc.273.22.13375. [PubMed: 9593664]

Masson GR, Perisic O, Burke JE, & Williams RL (2016). The intrinsically disordered tails of PTEN and PTEN-L have distinct roles in regulating substrate specificity and membrane activity. The Biochemical Journal, 473, 135–144. [PubMed: 26527737]

Miller S, Lou DY, Seldin DC, Lane WS, & Neel BG (2002). Direct identification of PTEN phosphorylation sites. FEBS Letters, 528, 145–153. [PubMed: 12297295]

Mingo J, Luna S, Gaafar A, Nunes-Xavier CE, Torices L, Mosteiro L, et al. (2019). Precise definition of PTEN C-terminal epitopes and its implications in clinical oncology. NPJ Precision Oncology, 3, 11. 10.1038/s41698-019-0083-4. [PubMed: 30993208]

Muir TW, Sondhi D, & Cole PA (1998). Expressed protein ligation: A general method for protein engineering. Proceedings of the National Academy of Sciences of the United States of America, 95(12), 6705–6710. 10.1073/pnas.95.12.6705. [PubMed: 9618476]

Nguyen HN, et al. (2014). Mechanism of human PTEN localization revealed by heterologous expression in Dictyostelium. Oncogene, 33, 5688–5696. [PubMed: 24292679]

Rahdar M, et al. (2009). A phosphorylation-dependent intramolecular interaction regulates the membrane association and activity of the tumor suppressor PTEN. Proceedings of the National Academy of Sciences of the United States of America, 106, 480–485. [PubMed: 19114656]

Salzmann M, Pervushin K, Wider G, Senn H, & Wüthrich K (1998). TROSY in triple-resonance experiments: new perspectives for sequential NMR assignment of large proteins. Proceedings of the National Academy of Sciences of the United States of America, 95(23), 13585–13590. 10.1073/pnas.95.23.13585. [PubMed: 9811843]

Santiago-Frangos A, Jeliazkov JR, Gray JJ, & Woodson SA (2017). Acidic C-terminal domains autoregulate the RNA chaperone Hfq. eLife, 6, e27049. 10.7554/eLife.27049. [PubMed: 28826489]

Sarbassov DD, Guertin DA, Ali SM, & Sabatini DM (2005). Phosphorylation and regulation of Akt/PKB by the rictor-mTOR complex. Science (New York, N.Y.), V307(5712), 1098–1101. 10.1126/science.1106148.

Shimada I (2005). NMR techniques for identifying the interface of a larger protein-protein complex: cross-saturation and transferred cross-saturation experiments. Methods in Enzymology, 394, 483–506. 10.1016/S0076-6879(05)94020-2. [PubMed: 15808234]

Trotman LC, et al. (2007). Ubiquitination regulates PTEN nuclear import and tumor suppression. Cell, 128, 141–156. [PubMed: 17218261]

van Zundert G, Rodrigues J, Trellet M, Schmitz C, Kastritis PL, Karaca E, et al. (2016). The HADDOCK2.2 web server: User-friendly integrative modeling of biomolecular complexes. Journal of Molecular Biology, 428(4), 720–725. 10.1016/j.jmb.2015.09.014. [PubMed: 26410586]

Vazquez F, Ramaswamy S, Nakamura N, & Sellers WR (2000). Phosphorylation of the PTEN tail regulates protein stability and function. Molecular and Cellular Biology, 20(14), 5010–5018. 10.1128/MCB.20.14.5010-5018.2000. [PubMed: 10866658]

Walker SM, Leslie NR, Perera NM, Batty IH, & Downes CP (2004). The tumour-suppressor function of PTEN requires an N-terminal lipid-binding motif. The Biochemical Journal, 379, 301–307. [PubMed: 14711368]

Williamson MP (2018). Chemical shift perturbation. In Webb G (Ed.), Modern magnetic resonance. Cham: Springer. 10.1007/978-3-319-28388-3_76.

Worby CA, & Dixon JE (2014). Pten. Annual Review of Biochemistry, 83, 641–669.

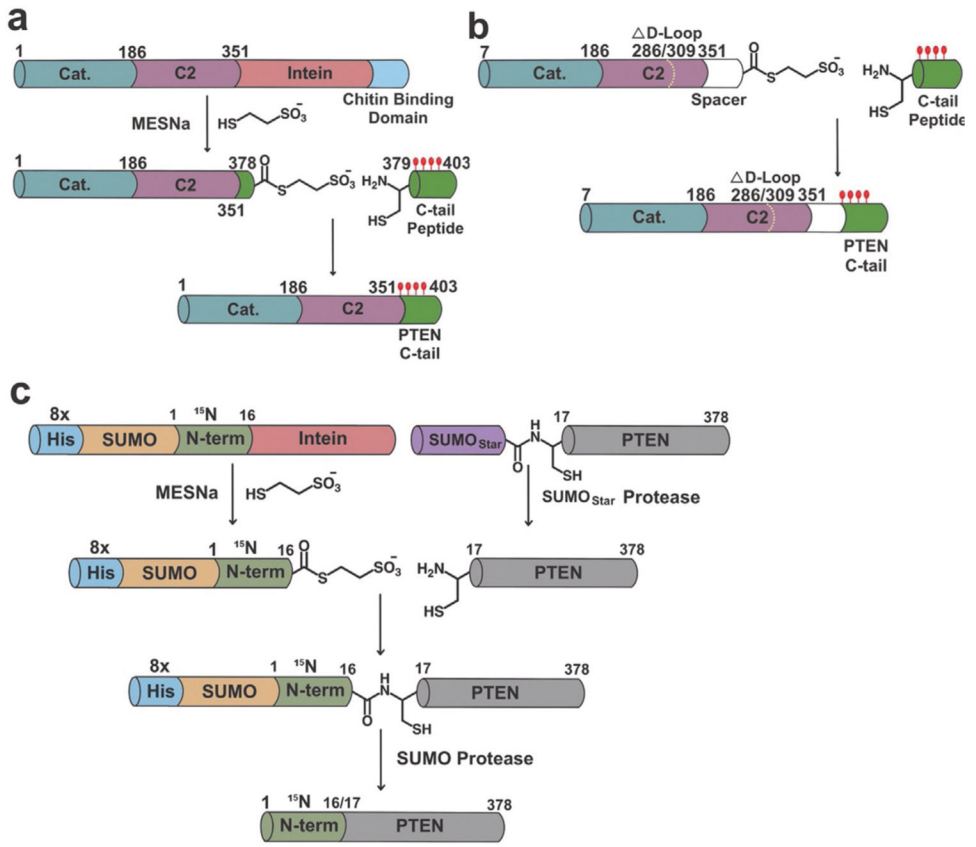

Fig. 1.

PTEN EPL. (A) Scheme showing the generation of semi-synthetic full-length phosphorylated PTEN by EPL. Red circles represent C-terminal phosphorylation sites. (B) Scheme showing generation of semi-synthetic crPTENs for testing the spacer length and protein X-ray crystallography. Red circles represent C-terminal phosphorylation sites. White dashed line represents the deletion of the D-loop (286–309) and white cylinder represents the artificial spacer. (C) Scheme showing the chemical ligation of the ^{15}N N-terminal 16 amino acids to PTEN to generate the segmentally labeled protein for NMR analysis.

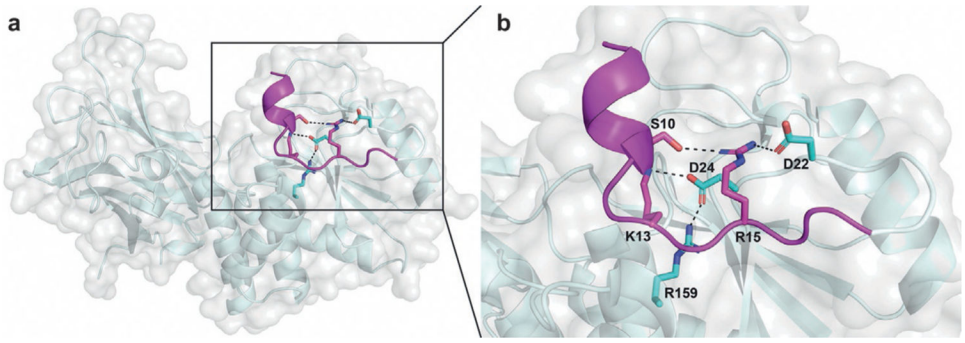

Fig. 2.

PTEN crystal structure with N-terminal 4p-crPTEN-13_{sp}-T1 (PDB 7JUL) where new N-terminal structure (Met6-Tyr16) is in magenta, including the N-terminal helix (Glu7-Asn12). (A) Zoomed out view of (B), Enlarged view of helix displaying hydrogen bond interactions of key residues (Ser10, Arg15, and Asp24) that stabilize the position of the helix. Hydrogen bonds is represented as dashed lines.

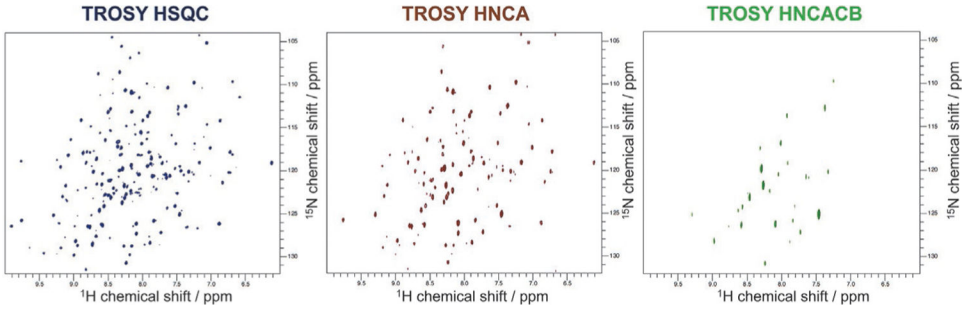

Fig. 3.

^{15}N-^{1}H-TROSY HSQC spectrum and ^{15}N-^{1}H projections of 3D TROSY HNCA and HN(CA)CB of ^{2}H-^{13}C-^{15}N VSP show the reduction of peak number with increasing experiment length and complexity.

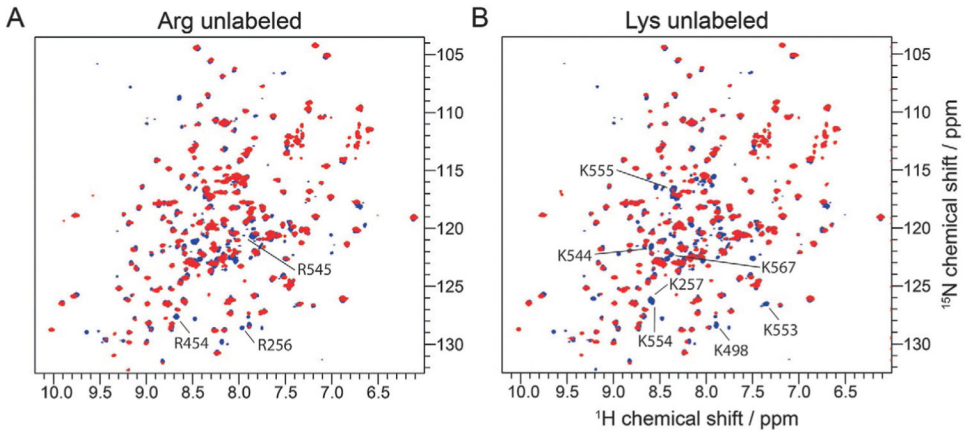

Fig. 4.

^{15}N-^{1}H-TROSY HSQC spectrum U-^{15}N VSP (blue) overlaid with spectra of ^{15}N VSP expressed using selective Arg (A) and Lys (B) unlabeling. Available peak assignments are shown.

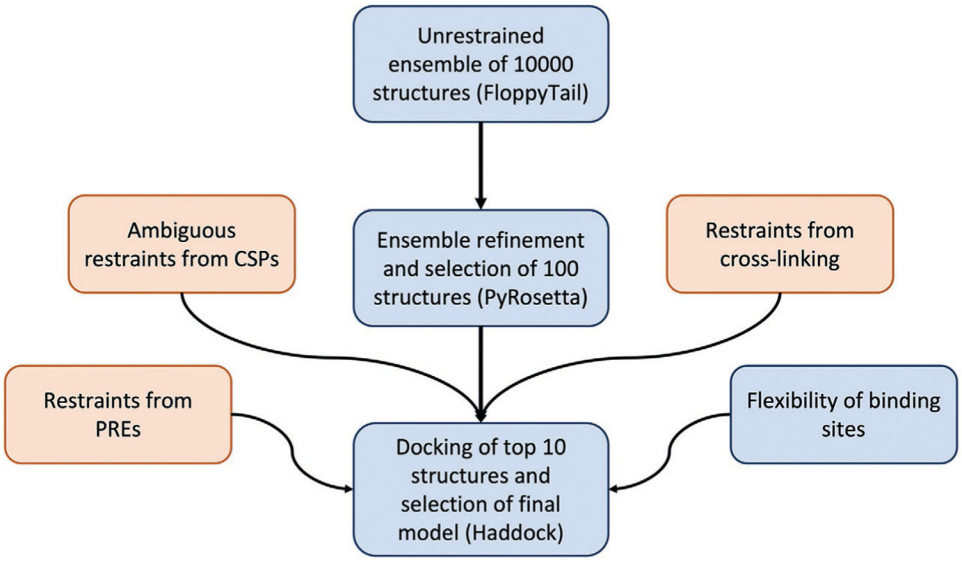

Fig. 5.

Workflow for modeling of VSP/C-tail interaction. Computational steps are shown in blue, experimental restraints in maroon.

Table 1

Reagents and materials for biochemical assays.

Reagent/material	Supplier	Catalog number
1,2-Dihexanoyl-sn-glycero-3-phospho-(1′-myo-inositol-3′,4′,5′-trisphosphate) (ammonium salt) (diC_6PIP_3)	Avanti Polar Lipids	850,176
Malachite Green Phosphate Detection Kit	R&D Systems	DY996
Alkaline Phosphatase Calf Intestinal (CIP)	New England Biolabs	M0290S
Phospho-PTEN (Ser380/Thr382/383) Rabbit mAb	Cell Signaling Technology	9549
Tris (2-Carboxyethyl) Phosphine Hydrochloride	Gold Biotechnology	TCEP25
Tris Base	Research Products International	T60040–500.0
Sodium 2-mercaptoethanesulfonate	Sigma-Aldrich	M3148
Sodium chloride	Chem-Impex	30070
Ovalbumin	Millipore Sigma	A2512
Bovine Serum Albumin (BSA)	Gemini Bio-Products	700–100P
iBlot Transfer Stack, nitrocellulose, mini	ThermoFisher Scientific	IB301002
Anti-rabbit IgG, HRP-linked Antibody	Cell Signaling Technology	7074
Amersham ECL Western Blotting Detection Reagent	Cytiva	RPN2106

Table 2

Procedure for diC6PIP3 enzyme activity assay.

1. Enzyme assay was performed in 25 μL of 50mM Tris pH8.0, 10mM BME, 50 μg/mL ovalbumin with varying concentrations of diC_6PIP_3 (0–160 μM) at 30 °C.
2. Reaction was initiated with 0.5–20 μg of PTEN and placed in a heat block set to 30 °C.
3. The reaction was diluted after a set time points (1–10min) with 25 μL of 50mM Tris pH8.0, 10mM BME and then immediately quenched with 10 μL of Buffer A from R&D Systems Malachite Green Phosphate Detection Kit (ammonium molybdate in 3M sulfuric acid). The quenched reaction was then incubated for 10min at room temperature.
4. 10 μL of Buffer B from R&D Systems Malachite Green Phosphate Detection Kit (malachite green oxalate and polyvinyl alcohol) was added next and incubated for 20min at room temperature.
5. Immediately after the 20-min incubation, the absorbance was measured at 620nm, which measures the free release of phosphate. The amount of free phosphate product produced per unit of time was determined by comparing the absorbance of the reaction to a standard curve made with varying concentrations of sodium phosphate using this same exact procedure.

Table 3

Procedure for alkaline phosphatase sensitivity assay.

1. Assay was performed at room temperature in 50mM Tris pH8.0, 10mM BME with 1 μM of 4p-PTEN or 4p-VSP. Reaction was initiated with 1 μM of calf intestinal alkaline phosphatase.
2. The reaction was quenched at several time points (0–240min) by adding 6 μL of the assay to 24 μL of 2× SDS-PAGE loading dye.
3. 5 μL of the quenched assay (50 ng of PTEN) was then run on a 10% SDS-PAGE gel and dry transferred to a nitrocellulose membrane using the iBlot system.
4. The nitrocellulose membrane was then incubated with 5% BSA in TBS for 1h at room temperature, and then with phospho-PTEN antibody diluted to 1:1000 in 2.5% BSA/TBST for 16h at 4 °C.
5. The membrane was then washed 3×'s with 10mL of TBST for 10min at room temperature. Then the membrane was incubated with 1:10,000 diluted 2° anti-rabbit-HRP antibody in 2.5% BSA/TBST for one hour at room temperature.
6. The membrane was then washed 2×'s with 10mL of TBST and then once with TBS for 10min at room temperature.
7. The loss of C-terminal tail phosphorylation was measured by chemiluminescence using Amersham ECL Western Blotting Detection Reagent. The intensity of Western blot bands was quantitated using ImageJ.

Table 4

Procedure for fluorescence binding assay.

1. Assay was performed in 150 μL of 50mM Tris pH8.0, 50mM NaCl, 1mM TCEP, 50ng/μL ovalbumin, 50nMF-4p-18mer-tail, and varying concentrations of PTEN or VSP proteins at 23 °C.
2. Fluorescence anisotropy measurements were collected with a Biotek Cytation 5 plate reader with an excitation wavelength of 495nm and emission wavelength of 520nm.

Table 5

Semi-synthetic PTENs generated for protein X-ray crystallography.

Name	Spacer Sequence	Synthetic peptide ligated	Crystallography conditions	PDB ID
n-crPTEN-13sp-T1	TGGGSGGTGGCRY	SDTTDSDPENEG	100mM Bis–Tris propane pH7.0, 1.2Mdl-malic acid	7JUL
4p-crPTEN-13sp-T2	TGGGSGGTGGCRY	SpDTpTpDSpDPENEG	100mM Bis–Tris propane pH7.0, 1.2Mdl-malic acid	7JUK
4p-crPTEN-20sp-T3	TGGGSGGTGGGSGGTGGGCY	SpDTpTpDSpDPENEPFDED	300mM sodium citrate tribasic, 20% (v/v) PEG 3350	7JVX
4p-crPTEN-22sp-T3	TGGGSGGTGGGSGGTGGGSGCY	SpDTpTpDSpDPENEPFDED	300mM sodium citrate tribasic, 20% (v/v) PEG 3350	7JTX

Table 6

Reagents and materials for PTEN insect cell expression and purification.

Reagent/material	Supplier	Catalog number
Sf 21 insect cells	ThermoFisher Scientific	11497013
High Five cells	ThermoFisher Scientific	B85502
Grace's Insect Medium, supplemented	ThermoFisher Scientific	11605094
Grace's Insect Medium, unsupplemented	ThermoFisher Scientific	11595030
Express Five SFM	ThermoFisher Scientific	10486025
Fetal Bovine Serum (FBS)	Millipore Sigma	F0926
L-Glutamine (200mM)	ThermoFisher Scientific	25030081
Antibiotic Antimycotic Solution (100×), Stabilized	ThermoFisher Scientific	A5955
T-25 tissue culture treated flask, vented cap, canted neck	Stellar Scientific	TC30–110
Cellfectin II Reagent	ThermoFisher Scientific	10362100
PureLink HiPure Plasmid Miniprep Kit	ThermoFisher Scientific	K210002
DH10Bac Competent Cells	ThermoFisher Scientific	10361012
S.O.C. Medium	ThermoFisher Scientific	15544034
LB Broth (Miller)	Millipore Sigma	L3522
2× YT medium	Millipore Sigma	Y2377
Agar		
Isopropyl-beta-D-thiogalactopyranoside	Gold Biotechnology	I2481C50
Kanamycin sulfate	Bio Basic Inc.	KB0286–5
Ampicillin, sodium salt	Bio Basic Inc.	AB0028
Gentamicin		
Tetracycline		
5-Bromo-4-chloro-3-indolyl β-D-galactopyranoside (X-gal)	Millipore Sigma	B4252
3L Adjustable Hanging Bar Flat Bottom Spinner Flask	BellCo Glass	1967–03000
Isopropyl-beta-D-thiogalactoside (IPTG)	GoldBio	I2481C
DL-Malic acid, pH7.0	Hampton Research	HR2–761
1.5M Sodium citrate tribasic dihydrate	Molecular Dimensions	MD2-100-127
50% *w*/*v* PEG 3350	Molecular Dimensions	MD2-100-9
1.0M BIS-TRIS propane pH7.0	Hampton Research	HR2–795
1,2-Dihexanoyl-sn-glycero-3-phospho-(1′-myo-inositol-3′,4′,5′-trisphosphate) (ammonium salt) (diC_6PIP_3)	Avanti Polar Lipids	850176
Malachite Green Phosphate Detection Kit	R&D Systems	DY996
Alkaline Phosphatase Calf Intestinal (CIP)	New England Biolabs	M0290S

Table 7

Procedure for PTEN and crPTEN insect cell expression (see Bac-toBac Baculovirus Expression System manual provided by Invitrogen), purification and expressed protein ligation.

1. *PTEN-GyrA intein-chitin binding domain* was subcloned into *pFASTBAC1* vector and transformed in DH10Bac competent cells. The transformed cells were grown on a LB agar plate containing 50 μg/mL kanamycin, 7 μg/mL gentamicin, 10 μg/mL tetracycline, 100 μg/mL X-gal, 40 μg/mL IPTG for 48h at 37 °C.
2. Several white colonies were then cultured in LB media supplemented with 50 μg/mL kanamycin, 7 μg/mL gentamicin, 10 μg/mL tetracycline overnight at 37 °C.
3. Each culture was then validated to have a bacmid with the PTEN gene inserted by PCR using pUC/M13 Forward and Reverse primers. The PCR product ranged from ~4200 to 4250 if PTEN was present.
4. The bacmid was then purified using PureLink HiPure Plasmid Miniprep Kit.
5. *Sf* 21 insect cells were cultured in supplemented Grace's Insect Medium with 10% FBS in a T75 flask until a density of 1–1.5 million/mL at 27 °C.
6. *Sf* 21 cells were then added a 6-well plate (800,000/well) and allowed to adhere for 15min at 27 °C. The media was then changed to have 85% of unsupplemented Grace's Insect Medium and 15% supplemented Grace's Insect Medium with 10% FBS.
7. 2 μg of bacmid was transfected into each well after incubating for 20–30min at room temperature with a mixture of 8 μL of Cellfection II and 200 μL of unsupplemented Grace's Insect Medium.
8. The transfected plate was then incubated for five hours at 27 °C and away from light.
9. The transfection media was removed and replaced with supplemented Grace's Insect Medium with 10% FBS and 1× Antibiotic Antimycotic solution and culture for 3–5days at 27 °C and away from light to make P1 virus. Check for positive signs of viral infections which include the cells swelling and detaching from plate.
10. After viral infection is observed, the cells are spun down at 1000rpm and the supernatant is collected. Then use 400 μL of supernatant to infect new T75 flasks of *Sf*21 cells at a density of 1–1.5 million/mL. Incubate infected flasks for 3–5 days at 27 °C and away from light to generate P2 virus.
11. During this time, High Five cells should be culturing in liquid suspension at 27 °C using Express Five SFM media supplemented with 2mML-glutamine and 1× Antibiotic Antimycotic solution. The density of the High Five cells needs to be maintained between 0.5 and 2 million/mL.
12. Infect High Five cells at desired volume with P2 virus at an MOI of 1 (~20mL of P2 virus per 1L of High Five cells at a density of 1 million/mL) and culture at 27 °C for 48 h. After 48 h, the cell culture is centrifuged at 2000rpm and the pellet stored at −80 °C until purification.
13. To begin PTEN purification, the pellet was then resuspended into 50mM HEPES pH7.5, 250mM NaCl, 1mM EDTA, 1mM TCEP, 10% glycerol, and one tablet of complete EDTA-free protease inhibitor cocktail (Pierce), lysed using 40 strokes with a Dounce homogenizer, and centrifuged at 15,000rpm at 4 °C for 40min.
14. The supernatant was then incubated with cellulose resin for 30 mins on ice to remove chitinase.
15. Then the chitinase depleted lysate was loaded onto chitin resin (5mL of resin per 1L of insect cell culture) at 4 °C, washed with 20 column volumes of 25mM HEPES pH7.5, 250mM NaCl, 1mM EDTA, 0.1% Triton, and then 10 column volumes of 50mM HEPES pH7.5, 250mM NaCl, 1mM EDTA.
16. The tail peptide was ligated onto PTEN by incubating the chitin resin with PTEN immobilized with 50mM HEPES pH7.5, 250mM NaCl, 1mM EDTA, 400mM MESNa, and 2mM of the corresponding peptide for 48–72h at room temperature.
17. The ligated product was then eluted from the column and dialyzed into 50mM Tris pH8.0, 5mM NaCl, 10mM DTT overnight at 4 °C.
18. The dialyzed sample was then loaded onto a GE MonoQ column and purified using a gradient of 0–50% buffer B over 240mL (Buffer A: 50mM Tris pH8.0, 5mM NaCl, 10mM DTT, Buffer B: 50mM Tris pH8.0, 1M NaCl, 10mM DTT). Purified fractions were analyzed by SDS-PAGE and dialyzed into 50mM Tris pH8.0, 200mM NaCl, 10mM DTT.
19. The dialyzed semi-synthetic PTEN was then further purified by injecting onto a gel filtration column (Superdex 200 or Superdex 75 column) using 50mM Tris pH8.0, 200mM NaCl, 10mM DTT. Pure fractions were analyzed by SDS-PAGE, concentrated, flash frozen, and stored at −80 °C. PTENs for protein X-ray crystallography were concentrated to 14–20mg/mL, whereas PTENs intended for biochemical analysis were concentrated to 1–4mg/mL.

Table 8

Key reagents and materials for the generate of ^{15}N-16mer-tPTEN.

Reagent	Supplier	Catalog number
Rosetta (DE3)pLysS Competent Cells	Millipore Sigma	70956
LB Broth (Miller)	Sigma-Aldrich	L3522
Isopropyl-beta-D-thiogalactopyranoside	Gold Biotechnology	I2481C50
Kanamycin sulfate	Bio Basic Inc.	KB0286–5
Sodium 2-mercaptoethanesulfonate	Millipore Sigma	M1511–5G
Ammonium chloride (15N, 99%)	Cambridge Isotope Laboratories, Inc	NLM-467–1
SUMOstar Protease	LifeSensors	SP4110
Chitin Resin	New England Biolabs	S6651L
Tris Base	Research Products International	T60040–500.0
4-(2-Hydroxyethyl)-1-piperazineethanesulfonic acid	Chem-Impex	00174
Sodium chloride	Chem-Impex	30070
Tris (2-Carboxyethyl) Phosphine Hydrochloride	Gold Biotechnology	TCEP25
Glycerol	Millipore Sigma	G5516
Pierce Protease Inhibitor Tablets, EDTA-free	ThermoFisher Scientific	A32965
pet-28a(+) vector	Millipore Sigma	69864

Table 9

Production of semi-synthetic N-terminally labeled PTEN.

1. Express two liters of PTEN N-terminal 8× His_{tag}-SUMO-$PTEN_{1–16}$-GryA intein-CBD 16 amino in *BL21(DE3) Rosetta pLysS E. coli* cells in M9 minimal media (see Table 10) supplemented with 40 μg/mL kanamycin and 1g/L [^{15}N] ammonium chloride. Inoculate 1L of minimal media with 5mL of overnight culture. Induce the cell culture at an OD_{600} of 0.6 with 0.5mM IPTG at 22 °C for 16h.
2. Harvest cells by centrifugation at 4000rpm at 4 °C and discard the supernatant.
3. Resuspend cell pellet in 50mM HEPES pH7.5, 250mM NaCl, 1mM EDTA, 1mM TCEP, 10% glycerol and one tablet of EDTA-free protease inhibitor cocktail.
4. Lyse cells by passing through French press (3xs), centrifuge at 15,000rpm at 4 °C for 30min, and load supernatant onto 20mL of chitin resin at 4 °C.
5. Wash column with 400mL of 25mM HEPES pH7.5, 250mM NaCl, 1mM EDTA, 0.1% Triton and then 200mL of 50mM HEPES pH7.5, 250mM NaCl, 1mM EDTA.
6. The resin was then incubated with 50mM HEPES pH7.5, 250mM NaCl, 1mM EDTA and 400mM MESNa for 24h at room temperature to generate ^{15}N-8×-His-SUMO-$PTEN_{1–16}$-MESNa thioester.
7. ^{15}N-8×-His-SUMO-$PTEN_{1–16}$-MESNa thioester was then eluted with 60mL of 50mM HEPES pH7.5, 250mM NaCl, 1mM EDTA, 1mM TCEP, the pH was decreased to 6.0 with 6M HCL, and concentrated with an Amicon 10kDa filter.
8. The chitin resin was then treated with more 50mM HEPES pH7.5, 250mM NaCl, 1mM EDTA and 400mM MESNa for another 24h at room temperature to improve the yield.
9. The other segment (PTEN-N$\Delta 16_{Q17C,\ Y379C}$) was expressed as an 8×-His-$SUMO_{star}$-PTEN-N$\Delta 16_{Q17C}$-GyrA intein-CBD fusion and immobilized to chitin resin using the same methods discussed in Table 7.
10. Then the chitin resin was treated with 50mM HEPES pH7.5, 250mM NaCl, 1mM EDTA, 400mM MESNa, and 50mM cysteine for 24h at room temperature to generate 8×-His-$SUMO_{star}$-PTEN-N$\Delta 16_{Q17C,\ Y379C}$.
11. The N-terminal 8×-His-$SUMO_{star}$ was then cleaved to reveal and N-terminal cysteine by treating the sample with 200 units SUMOstar Protease 1 for 16h at 4 °C while dialyzing into 50mM HEPES pH7.5, 200mM NaCl, 1mM TCEP.
12. Then 8×-His-$SUMO_{star}$ and SUMOstar Protease 1 was removed by passing the sample over Ni^{2+} Sepharose 6 Fast Flow resin and collecting the flowthrough. The resin was then washed with 10mL of 100mM HEPES pH7.5, 500mM NaCl, and 75mM imidazole and collected with the flowthrough.
13. The newly formed Cys-$PTEN_{17–379,\ Y379C}$ was then dialyzed into 50mM HEPES pH7.0, 200mM NaCl, 1mM TCEP for 16h at 4°C
11. To ligate the two segments, the ^{15}N-8×His-SUMO-$PTEN_{1–16}$-MESNa thioester was dialyzed three times (one hour per time) against 50mM HEPES pH7.8, 200mM NaCl, 1mM TCEP at 4°C.
12. Then both segments were combined with a final buffer concentration of 50mM HEPES pH7.8, 200mM NaCl, 1mM TCEP, 100mM MESNa and concentrated to where ^{15}N-8×His-SUMO-$PTEN_{1–16}$-MESNa was somewhere within 100–250 μM. The sample was placed at 4°C for three days, where on the second day more 8×-His-$SUMO_{star}$-PTEN-N$\Delta 16_{Q17C,\ Y379C}$ from 1L of culture was spiked into the reaction to help improve product conversion.
13. After the reaction achieved >70% conversion, SUMO protease (ULP1, molar ratio of 1:10) was added to the sample to remove the 8×His-SUMO tag for another 16h at 4°C.
14. Then the sample was purified by FPLC using a MonoQ and Superdex200 column as discussed in Table 7, followed by dialysis into 50mM Tris pH7.5, 50mM NaCl and 1mM TCEP for NMR analysis.

Table 10

Production of semi-synthetic 4p-VSP_{C363S}.

1. Express two liters of 8×-His-SUMO-VSP_{C363S}-GyrA intein-CBD in *BL21 (DE3) Rosetta pLysS E. coli* cells using M9 minimal medium (6 g/L Na_2HPO_4; 3g/L KH_2PO_4; 0.5 g/L NaCl; 2mM $MgSO_4$ (24 mg/L); 0.1mM $CaCl_2$ (11 mg/L); 2g/LU-$^{13}C_6$-*D*-glucose; 1g/L $^{15}NH_4Cl$; 40 μg/mL kanamycin; 10mg/L $FeCl_2$; 0.77mg/L $ZnCl_2$; 0.08mg/L $MnCl_2$; 0.04mg/L $CoCl_2$; 0.01mg/L $CuCl_2$; 0.44mg/L thiamine; 0.44mg/L nicotinamide; 0.44mg/L pantothenic acid; 0.44mg/L pyridoxine; 0.22mg/L riboflavin, 0.22mg/L para-aminobenzoic acid; 2.2 μg/L biotin; 2.2 μg/L folic acid). Inoculate 1L of minimal media with 10mL of overnight culture. Induce cell culture at an OD_{600} of 0.6 with 0.5mM IPTG at 16 °C for 16 h.
2. Harvest cells by centrifugation at 4000rpm at 4 °C and discard the supernatant.
3. Resuspend cell pellet in 100mM HEPES pH7.5, 500mM NaCl, 20mM imidazole, 1mM TCEP, 1mM PMSF, and one tablet of EDTA-free protease inhibitor cocktail.
4. Lyse cells by passing through French press (3×s), centrifuge at 15,000rpm at 4 °C for 30min, and load supernatant onto 5mL of Ni Sepharose 6 Fast Flow at 4 °C.
5. Wash resin with 25mL of 100mM HEPES pH7.5, 500mM NaCl, 20mM imidazole, 1mM TCEP and then with 40mL of 100mM HEPES pH7.5, 500mM NaCl, 60mM imidazole, 1mM TCEP.
6. 8×-His-SUMO-VSP_{C363S}-GyrA intein-CBD was then eluted in 20mL of 100mM HEPES pH7.5, 500mM NaCl, 250mM imidazole, 1mM TCEP and then concentrated to ~5mL using an Amicon 10-kDa filter.
7. 8×-His-SUMO-VSP_{C363S}-GyrA intein-CBD was then dialyzed into 50mM HEPES pH7.8, 100mM NaCl, 1mM TCEP at 4 °C for 16 h.
8. Then ULP1 (1:10M ratio), 100mM MESNa, and 500 μM tetraphosphorylated peptide was added to sample and incubated for 3–4days at 4 °C until the percent ligation of the tail was >70%.
9. The semi-synthetic 4p-VSP_{C363S} reaction was loaded onto a GE MonoQ column and purified using a gradient of 0–50% buffer B over 240mL (Buffer A: 50mM Tris pH8.0, 5mM NaCl, 10mM DTT, Buffer B: 50mM Tris pH8.0, 1M NaCl, 10mM DTT). Purified fractions were analyzed by SDS-PAGE and dialyzed into 50mM Tris pH8.0, 200mM NaCl, 10mM DTT.
10. The dialyzed semi-synthetic 4p-VSP_{C363S} was then further purified by injecting onto a gel filtration column (Superdex 200 or Superdex 75 column) using 50mM Tris pH8.0, 200mM NaCl, 1mM TCEP. Pure fractions were analyzed by SDS-PAGE, collected, and dialyzed into 50mM Tris pH7.5, 50mM NaCl, 1mM TCEP for 16h at 4°C. Then the 4p-VSP_{C363S} sample was concentrated to 2.5–5mg/mL for NMR analysis.